Modal analysis reveals imprint of snowflake shape on wake flow structures

Giorgia Tagliavini
giorgia.tagliavini@empa.ch

Empa - Swiss Federal Laboratories for Materials Science and Technology, Laboratory for Computational Engineering, Dübendorf, Switzerland https://orcid.org/0000-0003-2090-8190

Markus Holzner
Institute of Hydraulic Engineering and River Research (IWA), University of Natural Resources and Life Sciences, Vienna, Austria

Pascal Corso
ARTORG Center for Biomedical Engineering Research, University of Bern, Bern, Switzerland
https://orcid.org/0000-0001-7875-1080

Research Article

Keywords: Aerodynamics, Modal Analysis, Snowflake Falling Behavior, Wake Flow Features

Posted Date: July 11th, 2024

DOI: https://doi.org/10.21203/rs.3.rs-4716383/v1

Additional Declarations: The authors declare no competing interests.

Modal analysis reveals imprint of snowflake shape on wake flow structures

Giorgia Tagliavini[1,2*], Markus Holzner[3,4,5], Pascal Corso[6]

[1] Empa - Swiss Federal Laboratories for Materials Science and Technology, Laboratory for Computational Engineering, Dübendorf, Switzerland

[2] PSI - Paul Scherrer Institut, Computational Fluid Dynamics Group, Villigen, Switzerland

[3] Institute of Hydraulic Engineering and River Research (IWA), University of Natural Resources and Life Sciences, Vienna, Austria

[4] WSL - Swiss Federal Institute for Forest, Snow and Landscape Research, Birmensdorf, Switzerland

[5] Eawag - Swiss Federal Institute for Aquatic Science and Technology, Dübendorf, Switzerland

[6] ARTORG Center for Biomedical Engineering Research, University of Bern, Bern, Switzerland

* e-mail: *giorgia.tagliavini@empa.ch*

Abstract

This study investigates the complex interplay of wake flow structures, particle shape, and falling behavior of snowflakes through advanced flow analysis. We employ Proper Orthogonal Decomposition and Dynamic Mode Decomposition to analyze the wake flow patterns of three distinct snowflake geometries at Reynolds number of 1500: a dendrite crystal, a columnar crystal, and a rosette-like particle. Proper Orthogonal Decomposition reveals that spatial resolution significantly impacts the capture of flow structures, particularly for particles with with more intricate wake flow structure, corresponding to unstable falling motion. Dynamic Mode Decomposition demonstrates high sensitivity to temporal resolution, with data of the forces exerted on the snowflake incorporated in the matrix prior to the decomposition mitigating information loss at lower sampling rates. We establish a linear relationship between snowflake shape porosity and minimum and maximum Dynamic Mode Decomposition eigenfrequencies, absolute decay or growth rates, and wavenumbers of the most energetic mode, linking particle geometry to wake flow characteristics. Higher porosity corresponds to more stable, small-scale flow structures and steady falling motion, while lower porosity promotes larger, unstable structures and falling trajectories with random particle orientations. These findings reveal the interdependence of snowflake geometry, wake flow configuration, and falling behavior and highlight the importance of considering both spatial and temporal resolutions when dealing with modal analysis. This research contributes to improved predictions of snowflake falling behavior, with potential applications in meteorology and climate science.

Keywords: Aerodynamics, Modal Analysis, Snowflake Falling Behavior, Wake Flow Features.

1 Introduction

In weather prediction, the orientation of snow crystals during free-fall plays a pivotal role (Geier and Arienti, 2014). Together with snowflake fall speed, it impacts snowfall and the subsequent distribution of snow on the ground (Aguirre et al., 2018; Bender et al., 2020; Li et al., 2021). In nature, snowflakes exhibit a wide range of geometries and sizes (Bailey and Hallett, 2009; Kikuchi et al., 2013). For large snow particles ($D_{\max} \gtrsim 100$ μm), their particle Reynolds number ($Re = u_t D_{\max}/\nu \gg 1$, where $D_{\max}$ represents the particle's maximum extension orthogonal to the flow direction [m], u_t is the snowflake's terminal velocity magnitude [m/s], and ν is the kinematic viscosity of air [m^2/s]) deviates from the Stokesian regime ($Re \ll 1$) (Libbrecht, 2005; Westbrook, 2008). This, together with snowflake irregular shapes, gives rise to complex falling motion with intricate trajectories (Gunn and Marshall, 1957; Nemes et al., 2017; McCorquodale and Westbrook, 2020b).

Understanding the elaborate free-falling dynamics of snowflakes necessitates a comprehensive exploration of the interplay between wake flow, snowflake shape, and particle aerodynamics. Particle wake flow exerts a substantial influence on its drag and overall falling behavior (Adrian, 1991; Giles and Cummings, 1999; Auguste et al., 2013; Singh et al., 2023). Previous research has extensively studied the wake flow structures behind simple particle geometries such as spheres (Uhlmann and Dusek, 2014; Emadzadeh and Chiew, 2020), cylinders (Toupoint et al., 2019), disks (Field et al., 1997; Kim et al., 2018), planar polygons (Esteban et al., 2019), and polyhedra (Trunk et al., 2021; Gai and Wachs, 2024). Only a few studies have ventured into investigating the wake flow behind complex-shaped objects and the effect of shape features, such as shape porosity and sphericity, on drag and particle falling behavior (Nediç et al., 2015; Cummins et al., 2018; McCorquodale and Westbrook, 2020b). Our past work (Tagliavini, 2022) delved into the interplay between wake flow features, drag coefficient, and falling behavior of realistic snow particles using Delayed-Detached Eddy Simulations (DDES) on fixed snowflakes subjected to airflow. This approach, validated for the prediction of the particles' drag coefficients and fall speeds (Tagliavini et al., 2021a) against experimental data of 3D-printed snowflake analogs falling in a vertical water tank (McCorquodale and Westbrook, 2020b), was further extended by Tagliavini et al. (2021b) through a comprehensive analysis of wake flow organization, momentum flux decomposition, and their relation with the drag acting on the snow particles. While the analysis highlighted vortex dynamics in the wake flow of complex-shaped snow particles, the question regarding the dominant flow structures in the particle wake, as well as their impact on the particle falling behavior, remained open.

To address the challenges posed by intricate flow patterns and high-order dynamics, such as those present in the wake flow of complex-shaped particles, it has become established to simplify such flows using modal decomposition techniques (Cherubini et al., 2021; Huang et al., 2022; Yu and Durgesh, 2022). These data-driven methodologies, including Proper Orthogonal Decomposition (POD) (Lumley, 1967) and Dynamic Mode Decomposition (DMD) (Schmid, 2010), are effective in capturing energetically and dynamically significant features of a given flow field, primarily velocity or vorticity fields (Menon and Mittal, 2020; Corso et al., 2021). These techniques yield spatial flow features, called *modes*, accompanied by characteristic values indicative of energy content, decay or growth rates, and frequencies (Tu et al., 2014). However, to the best of our knowledge, these techniques have not yet been applied to explore the wake flow of complex-shaped snow particles.

In the present study, we first aim to evaluate the impact of spatial and temporal filtering of flow data sets on the accuracy of POD and DMD results. To achieve this, the streamwise velocity u_x is taken into account due to its capability of capturing the primary flow dynamics, such as flow separation and coherent structures within the wake flow, which are critical for understanding drag and lift forces. Furthermore, the choice of one velocity component makes the calculation less computationally demanding. We perform Proper Orthogonal Decomposition on two distinct numerical data sets: the streamwise velocity field in the wake from simulations of fixed, complex-shaped snow particles at $Re = 1500$ (spatial resolution of approximately 10^{-4} m), and the same wake velocity field at the same Re spatially resampled to match the resolution of experimental flow data (spatial resolution of approximately 0.002 m (McCorquodale and Westbrook, 2020a)). Subsequently, Dynamic Mode Decomposition is performed on the computational streamwise velocity field and on the same field with the forces acting on the snow particle added to the snapshot matrix. By including both streamwise velocity and force data, it is possible to assess the imprint of forces exerted on the particle onto the wake flow through the DMD analysis. This leads to a deeper understanding of the causal relationships at play in snow particle aerodynamics. In the final part of our study, a correspondence between the extracted temporal and spatial features from the DMD, the snowflake shape, and the snow particle falling behavior is established and discussed.

This paper presents the following structure. In Section 2.1, we briefly describe the experimental set-up and observations that informed our numerical model, whose description follows in Section 2.2. The theory underlying Proper Orthogonal Decomposition and Dynamic Mode Decomposition is explained in Section 2.3. Then, the type of data sets and the methods employed for the analysis of the data are presented in Section 2.4. We finally discuss the results in Section 3.

2 Materials and methods

In this section, a concise overview of experimental set-up and observations that informed and allowed to validate our numerical model is provided (Section 2.1). We then summarize the key aspects of the numerical model in Section 2.2, and we offer a brief exposition of the theory underlying Proper Orthogonal Decomposition and Dynamic Mode Decomposition (Section 2.3). Lastly, Section 2.4 examines the type of data and the methods employed to analyze the results.

2.1 Particle orientations from 3D-printed snowflake analogs' experiments

The experiments involve the release of 3D-printed snowflake analogs in a vertical tank containing a viscous fluid. Measurements of instantaneous flow velocities are obtained using synchronized cameras and a dedicated algorithm (McCorquodale and Westbrook, 2020a). Precise tracking of falling analogues is achieved, allowing for the reconstruction of time-resolved trajectories and orientations (spatial resolution: ≈ 0.15 cm). From a variety of snow particle shapes examined (McCorquodale and Westbrook, 2020b), three distinctive shapes, among those employed in the experiments, are selected for this study: a plate-like dendrite crystal **D1** (D1007), a capped-column **CC** (CC20Hex4), and rosette crystals **MR** (MR172). These three shapes are representative of realistic snowflake classes found in nature (Kikuchi et al., 2013).

From the experimental data we obtain information about the inflow velocity and the particle orientation relative to the flow direction which are crucial for setting up the computational model. Figure A1 in the Supplementary Material illustrates the final orientations of **D1**, **CC**, and **MR** (in black). These orientations are taken from the laboratory observations after the particle has been falling for a certain amount of time and has reached a quasi-stable motion. It is clear that, for particles with unsteady falling behavior, a quasi-stable falling condition is difficult to determine. As a consequence, alternative orientations are selected for particle **CC** and **MR**. In particular, we define two extreme orientations that represent two extreme positions that these geometries frequently adopt during free fall, as illustrated in Figure A1(b, c) (Tagliavini et al., 2021b). A full description of the wake flow and falling behavior of each snow particle is presented in Section 3.1 to assist the reader in fully understanding the results.

2.2 Delayed-Detached Eddy Simulations

The computational model of the 3D fixed snow particle is based on a hybrid RANS-LES approach known as Delayed-Detached Eddy Simulation (DDES) (Spalart et al., 2006). The DDES model employs the Spalart–Allmaras turbulence closure to evaluate the eddy viscosity $\tilde{\nu}$ for the RANS calculation (Spalart and Allmaras, 1994). It is implemented in OpenFOAM 4.1 (Open source Field Operation And Manipulation), a C++ software built upon the finite volume method (OpenFOAM, 2017). The transient, incompressible Navier-Stokes equations govern the airflow motion:

$$\begin{aligned} \boldsymbol{\nabla} \cdot \boldsymbol{u} &= 0, \\ \rho \left(\frac{\partial \boldsymbol{u}}{\partial t} + (\boldsymbol{u} \cdot \boldsymbol{\nabla}) \boldsymbol{u} \right) &= -\boldsymbol{\nabla} p + \mu \boldsymbol{\nabla}^2 \boldsymbol{u} + \rho \boldsymbol{f}, \end{aligned} \tag{1}$$

where $\boldsymbol{u}$ is the flow velocity [m/s], ρ is the fluid density [kg/m^3], p is the pressure [Pa], μ is the dynamic viscosity of the fluid [Pa·s], and $\boldsymbol{f}$ represents external forces per unit mass [N/kg]. The forces acting on the particle, with normal and tangential contributions, can be expressed as:

$$\boldsymbol{F} = \boldsymbol{F}_p + \boldsymbol{F}_\nu = \int_S p\, \boldsymbol{n}\, dS + \int_S \tau\, \boldsymbol{n}\, dS, \tag{2}$$

where $\boldsymbol{n}$ is the normal unit vector on the particle surface S, and τ denotes the viscous stress tensor [Pa]. At the inlet, a uniform air velocity is imposed and computed using:

$$u_\infty = \frac{Re\, \nu}{D_{\max}}. \tag{3}$$

Here, Re stands for the desired particle Reynolds number, $D_{\max}$ represents the maximum dimension of the particle (i.e., the largest dimension of the snow particle normal to the flow direction) [m], u_∞ denotes the uniform inlet velocity [m/s], and ν represents the kinematic viscosity of air [m^2/s]. The domain and grid size of the computational model are depicted in Figure A2. All simulations run at $Re = 1500$ and at least for five flow through times to ensure a fully developed wake flow behind the object (Durbin and Medic, 2007). For more details on the validation, the grid convergence study, the turbulence modeling, and the numerical schemes, the reader is referred to Tagliavini et al. (2021a).

2.3 Modal analysis of the wake flow field

Modal analysis techniques, such as Proper Orthogonal Decomposition (POD) and Dynamic Mode Decomposition (DMD), are powerful tools extensively used in fluid dynamics to understand and extract dominant features from complex flow fields (Tu et al., 2014; Kutz et al., 2015; Cherubini et al., 2021; Huang et al., 2022). POD and DMD make use of a snapshot matrix. This matrix contains information about the investigated field at different time instants stored as column vectors in chronological order:

$$\mathbf{X} = [\mathbf{x}(\boldsymbol{\zeta}, t_1), \mathbf{x}(\boldsymbol{\zeta}, t_2), ..., \mathbf{x}(\boldsymbol{\zeta}, t_m)] \in \mathbb{R}^{n \times m}, \tag{4}$$

where $\boldsymbol{\zeta}$ denotes the spatial coordinate vector and $\boldsymbol{x}$ is a vector field (in our case the streamwise velocity), while $t_1, ..., t_m$ are the time instants sampled at an interval Δt (see Section 2.4). POD and DMD are based upon Singular Value Decomposition (SVD) of the snapshot matrix. SVD can be employed to obtain optimal low-rank matrix approximations and is formulated as follows. Let us consider a set of complex quantities $\boldsymbol{v}_k \in \mathbb{C}^n$, $\boldsymbol{A} \in \mathbb{C}^{m \times n}$, and $\boldsymbol{q}_j \in \mathbb{C}^m$. We can write in matrix form:

$$\mathbf{AV} = \mathbf{Q\Sigma}, \tag{5}$$

with $\boldsymbol{V} = [\boldsymbol{v}_1, ..., \boldsymbol{v}_n] \in \mathbb{C}^{n \times n}$, $\boldsymbol{Q} = [\boldsymbol{q}_1, ..., \boldsymbol{q}_m] \in \mathbb{C}^{m \times m}$, and $\boldsymbol{\Sigma} \in \mathbb{R}^{m \times n}$ a matrix with $\sigma_1 \geqslant \sigma_2 \geqslant ... \geqslant \sigma_g \geqslant 0$ along its diagonal ($g = min(m, n)$) and zero elsewhere. Isolating the $\boldsymbol{A}$ matrix, multiplying the right-hand side of Equation (5) by the conjugate transpose $\boldsymbol{V}^*(= \boldsymbol{V}^{-1})$, we obtain:

$$\mathbf{A} = \mathbf{Q\Sigma V}^*. \tag{6}$$

2.3.1 Proper Orthogonal Decomposition

Proper Orthogonal Decomposition (POD) was first introduced by Lumley (1967). In fluid dynamics, it became a common technique to extract coherent flow structures to characterize turbulence-related phenomena (Leask and McDonell, 2019). POD provides the best approximation of the original data in the least-squares sense for any given number of modes r. This can be expressed mathematically as:

$$\min_{\phi_i^{POD}} \sum_{j=1}^{M} \left| \mathbf{x}(\zeta_j, t_j) - \underbrace{\sum_{i=1}^{r} \alpha_i^{POD}(t_j)\boldsymbol{\phi}_i^{POD}}_{\mathbf{X}(\boldsymbol{\zeta},t)} \right|^2 , \tag{7}$$

where M is the total number of time steps and $\mathbf{X}(\boldsymbol{\zeta}, t)$ is the approximated field, in which the time coefficients α_i^{POD} are obtained by projecting the original field onto the space spanned by the POD modes ($\alpha_i^{POD}(t) = (\boldsymbol{\phi}_i^{POD})^T \boldsymbol{x}(t)$), and $\boldsymbol{\phi}_i^{POD}$ are the POD modes that carry the spatial information. The minimization performed by POD ensures that for any truncation level r, the POD modes provide the most efficient representation of the data in terms of captured energy.

We take into consideration the snapshot matrix $\boldsymbol{X}$ as defined in Equation 4 and apply an eigendecomposition to the correlation matrix $\boldsymbol{R} = \boldsymbol{X}\boldsymbol{X}^T \in \mathbb{R}^{n\times n}$. We then obtain the eigenvectors and eigenvalues $\boldsymbol{\phi}_i^{POD}$ and μ_i^{POD}, respectively. Therefore, it is possible to formulate:

$$\mathbf{R}\boldsymbol{\Phi}^{POD} = \mathcal{M}^{POD}\boldsymbol{\Phi}^{POD} , \tag{8}$$

with $\boldsymbol{\Phi}^{POD} = [\boldsymbol{\phi}_1^{POD}, ..., \boldsymbol{\phi}_n^{POD}]$ and $\mathcal{M}^{POD} = [\mu_1^{POD}, ..., \mu_n^{POD}]$. Each eigenvalue μ_i^{POD} represents how much the energy contained in each mode $\boldsymbol{\phi}_i^{POD}$ captures the energy of the original field. The error associated with the truncation to r modes can be quantified using the eigenvalues:

$$\epsilon_r = \frac{\sum_{i=r+1}^{m} \mu_i^{POD}}{\sum_{i=1}^{M} \mu_i^{POD}} . \tag{9}$$

This error measure allows to choose the number of modes that balance between model dimensionality reduction and accuracy. In fact, retaining only the most energetic modes, POD can significantly reduce the dimensionality of the problem while minimizing the loss of important flow features (Tu et al., 2014; Taira et al., 2017).

2.3.2 Dynamic Mode Decomposition

Dynamic Mode Decomposition (DMD) operates by decomposing time-resolved data to identify coherent spatio-temporal patterns, their growth rates, and their frequencies. Since its introduction by Schmid (2010), many different variations of the algorithm have been proposed (Belson et al., 2014; Vega and Le Clainche, 2017; Krake et al., 2019). As compared to POD, it provides additional information about the temporal behavior of the decomposed data considering the best-fitting linear operator $\boldsymbol{A}$ to approximate the dynamics of a system:

$$\frac{\partial \mathbf{x}(t)}{\partial t} = \mathbf{A}\mathbf{x}(t)\,, \tag{10}$$

whose solution is:

$$\mathbf{x}(t) = e^{\mathbf{A}\mathbf{x}(t)}\,\mathbf{x}(0)\,, \tag{11}$$

in which $\boldsymbol{x}(0)$ represent the solution of the system at $t = 0$ s. DMD approximates the snapshot matrix $\boldsymbol{X}$ (Equation (4)) with a set of eigenvectors and eigenvalues, which carry the spatial and temporal information of the system, respectively. To perform Dynamic Mode Decomposition, the matrix $\boldsymbol{X}$ is split in two matrices $\boldsymbol{X_1}$ and $\boldsymbol{X_2}$ which are the non-time-advanced and the time-advanced matrix, respectively. $\boldsymbol{X_1}$ incorporates the snapshots from t_1 to t_{m-1}, whereas $\boldsymbol{X_2}$ the snapshots from t_2 to t_m, where m is the number of time instants considered for the temporal sampling. Therefore, the dynamic system can be expressed as:

$$\begin{aligned} \mathbf{X}_2 &= \mathbf{A}\mathbf{X}_1\,, \\ \mathbf{A} &= \mathbf{X}_2\mathbf{X}_1^{+}\,, \end{aligned} \tag{12}$$

with $\boldsymbol{X}_1^{+}$, the Moore–Penrose pseudo-inverse of $\boldsymbol{X}_1$. First, the SVD is carried out on $\boldsymbol{X}_1$:

$$\mathbf{X}_1 = \mathbf{Q}\boldsymbol{\Sigma}\mathbf{V}^{*}\,. \tag{13}$$

Then, if we truncate the SVD by taking into account only the first r columns of $\boldsymbol{Q}$ and rows of $\boldsymbol{V}$, and the first r rows and columns of $\boldsymbol{\Sigma}$ (i.e., $\boldsymbol{Q}_r$, $\boldsymbol{V}_r$, and $\boldsymbol{\Sigma}_r$), we get:

$$\tilde{\mathbf{A}} = \mathbf{Q}_r^T\mathbf{X}_2\mathbf{V}_r\boldsymbol{\Sigma}_r^{-1}\,, \tag{14}$$

where $\tilde{\boldsymbol{A}}$ is the reduced-rank matrix of $\boldsymbol{A}$. Through eigendecomposition we have:

$$\tilde{\mathbf{A}}\mathcal{W} = \mathcal{M}^{DMD}\mathcal{W}\,, \tag{15}$$

where $\mathcal{M}^{DMD}$ is the diagonal matrix containing the DMD eigenvalues, μ_i^{DMD}, and the columns of $\mathcal{W}$ are the eigenvectors of the reduced-rank matrix $\tilde{\boldsymbol{A}}$. To retrieve the DMD modes (eigenvectors) of matrix $\boldsymbol{A}$, we use:

$$\boldsymbol{\Phi}^{DMD} = (\mathcal{M}^{DMD})^{-1}\mathbf{X}_2\mathbf{V}_r\boldsymbol{\Sigma}_r^{-1}\mathcal{W}\,. \tag{16}$$

that is the matrix containing the DMD modes, which carry the spatial information of the linear operator characterizing the dynamical system. If we define the exponential eigenvalues as $\lambda_i^{DMD} = \log(\mu_i^{DMD})/(\Delta t)$, the reconstruction of the analyzed field from DMD eigenvectors and eigenvalues is given by:

$$\mathbf{X}(\zeta, t) = \boldsymbol{\Phi}^{DMD} e^{(\boldsymbol{\Lambda}^{DMD}\Delta t)}\mathbf{C}\,, \tag{17}$$

in which $\boldsymbol{C} = (\boldsymbol{\Phi}^{DMD})^T\boldsymbol{X}_1$ contains the modal amplitudes, which scale each DMD mode based on its initial contribution to the system (at time $t = 0$), i.e. the amplitudes indicates how strongly each mode influences the initial conditions. In Equation (17), $\boldsymbol{\Lambda}^{DMD}$ is the diagonal matrix of the exponential eigenvalues λ_i^{DMD}. The introduction of the latter allows for establishing a correspondence between Equation (17) and Equation (11). The DMD eigenvalues come in conjugate pairs and are complex numbers defined as $\mu_i^{DMD} = a_i + jb_i$ (with a_i and b_i the real and the imaginary part, respectively, and $j = \sqrt{-1}$), and can be used to express:

$$\mu_i^{DMD}(t) = e^{\Re(\lambda_i^{DMD})\Delta t} \cdot e^{j\Im(\lambda_i^{DMD})\Delta t}\,. \tag{18}$$

Based on this definition we can derived the following quantities (De Schryver, 2016; Taira et al., 2017):

- exponential eigenvalue: $\lambda_i^{DMD} = \frac{\log(\mu_i^{DMD})}{\Delta t}$;

- modulus: $|\mu_i^{DMD}| = \rho_i = \sqrt{a_i^2 + b_i^2}$ which defines the mode evolution in time ($|\mu_i^{DMD}| = 1$ for stationary behavior, $|\mu_i^{DMD}| < 1$ in case of decay, and $|\mu_i^{DMD}| > 1$ for a growing mode);

- absolute decay or growth rate: $\sigma_i = \Re(\lambda_i^{DMD})$;

- relative decay rate: $\psi_i = \frac{\sigma_i}{\omega_i}$;

- angular frequency: $\omega_i = \Im(\lambda_i^{DMD})$;

- eigenfrequency: $\gamma_i = \frac{\omega_i}{2\pi}$.

While both POD and DMD serve the purpose of extracting meaningful modes from flow data, they have distinct characteristics and applications. POD primarily focuses on spatial structures and energy content, providing a low-dimensional representation of the dominant flow patterns. In contrast, DMD lays emphasis on the temporal dynamics and frequency content of the flow field, enabling the analysis of transient behavior and the identification of oscillatory (growing or decaying) phenomena (De Schryver, 2016; Taira et al., 2017). In this work, the Python library *modred* 2.1.0 developed by Belson et al. (2014) is employed, which allows for parallel computation of both POD and DMD. The library is adapted to accommodate our needs regarding the data analysis without substantial changes to the original algorithm.

2.4 Data sets, modal quantities, and particle shape descriptors

In our work, different data sets are analyzed to investigate the influence of diverse types of data on the modal analysis output and to identify the underlying wake flow patterns past complex-shaped snow particles. The data include:

- Data set ***S1***: streamwise velocity field (u_x) from Delayed-Detached Eddy Simulation (DDES) of a fixed snowflake (**D1**, **CC**, and **MR**, see Section 2.1) at a Reynolds number of 1500. We collect the u_x field within the wake using two different sampling rates: 1000 Hz (Δt_1) and 500 Hz (Δt_2). The highest sampling rate comes from the saved time steps of our numerical model, while the second is taken as half of the first one.

- Data set ***S2***: the previous velocity field u_x is spatially resampled on a larger grid to mimic the experimental resolution of 2 mm (see Section 2.1), allowing us to assess the impact of the spatial resolution on the modal analysis output. For the resampled data, only Δt_1 is used as snapshot sampling frequency.

- Data set ***S3***: for this third data set, the streamwise velocity field u_x is combined with the forces acting on the snow particle in the x, y, and z direction, calculated from the numerical simulations. These data offer a more complete collection of information concerning the snowflake wake flow structures that are indiscernible from the forces acting on the snow particle.

To extract dominant coherent structures and assess the influence of spatial resolution, we apply Proper Orthogonal Decomposition to ***S1*** and ***S2***. To better quantify the influence of spatial resolution, we perform a spatial Fast Fourier Transform using Welch's algorithm (Welch, 1967), with 256 sample points per segment, 50% overlap between segments, and a Hann windowing. To perform the FFT on the first and second POD mode, their spatial signals (streamwise velocity field u_x) are sampled along five lines within the particle wake with 2000 sampling point each line, as illustrated by Figure A3 of the Supplementary Material. The POD mode signals at each point of the sampling line are then averaged, and the FFT is applied to the resulting spatially averaged signal. We obtain the spatial Power Spectral Density (PSD(κ)) estimation as:

$$\mathrm{PSD}(\kappa) = \frac{1}{N_\zeta \mathcal{U}_\zeta} \left| \mathrm{FFT}\left[\overline{\mathbf{\Phi}}_i^{POD} \right] \right|^2 , \tag{19}$$

where $\overline{\mathbf{\Phi}}_i^{POD}$ represents the averaged signal from sampled POD modes spatially averaged over the five lines, κ denotes the wavenumber [1/m], and N_ζ is the number of points per segment, and $\mathcal{U}_\zeta$ is the normalization factor related to the window function.

In the second part of this study, Dynamic Mode Decomposition is performed on data ***S1*** and ***S3***. The modes are ordered based on the energy criterion proposed by Tissot et al. (2014). This ordering criterion prioritizes the modes capturing the majority of the energy content E_i^{DMD} within the snow particle wake, providing a more accurate representation of the dominant flow structures:

$$E_i^{DMD} = |c_i| \frac{e^{(2\sigma_i T)} - 1}{2\sigma_i T} , \tag{20}$$

in which $|c_i|$ is the magnitude of the modal amplitude of the i-th mode, taken from matrix $\boldsymbol{C} = (\mathbf{\Phi}^{DMD})^T \boldsymbol{X}_1$, σ_i is the absolute decay or growth rate, and T is the total sampling time [s] (in our case equal to 1 s). Equation (20) introduces a new method for selecting the most influential DMD modes based on a combination of their amplitude and their growth rate over a specified time period T. For the mode selection, we evaluate the normalized value of the energy as:

$$(E_i^{DMD})^* = \frac{E_i}{max(E_i)} \,. \tag{21}$$

After ordering the modes, the spatial and temporal signals from DMD are analyzed. Regarding the spatial signal, we employ the averaging operation over five lines (Figure A3 in the Supplementary Material) as for the POD, using Equation (19) and substituting $\overline{\mathbf{\Phi}}_i^{POD}$ with $\overline{\mathbf{\Phi}}_i^{DMD}$ to get the spatial FFTs of the first four DMD modes, ordered according to previously presented energy criterion. Subsequently, the temporal dynamics is also investigated. To do so, the temporal signal of the first 100 DMD modes is reconstructed as follows:

$$\mathbf{X}_{\mathrm{rec}}^{DMD}(t) = \sum_{i=1}^{100} c_i\, e^{\sigma_i\, \Delta t} \cdot e^{j\, \omega_i\, \Delta t} \,, \tag{22}$$

with c_i, σ_i, and ω_i defined in Section 2.3.2. The signal $\boldsymbol{X}_{\mathrm{rec}}^{DMD}(t)$ from Equation (22) is then incorporated in Welch's algorithm to obtain the temporal power spectral density (PSD(f)):

$$\mathrm{PSD}(f) = \frac{1}{N_t \mathcal{U}_t} \left| \mathrm{FFT}\left[\mathbf{X}_{\mathrm{rec}}^{DMD}(t) \right] \right|^2 \,, \tag{23}$$

where f denotes the frequency [1/s], N_t is the number of time points per segment, and $\mathcal{U}_t$ is the normalization factor related to the window function.

To appraise the influence of the particle shape on the wake flow, the same geometrical features as in Tagliavini et al. (2021b), namely the particle's shape porosity and Corey's shape factor (Corey, 1949), are employed. Since only the porosity ϵ showed a consistent correlation to the quantities from the modal analysis, we report its definition here below:

$$\epsilon = 1 - A_R, \tag{24}$$

where A_R is defined as $A_R = A_p/A_{disk}$, with A_p being the particle frontal area and A_{disk} the area of the enclosing disk [m^2]. The shape porosity of the three investigated snow particles is 0.62, 0.51, and 0.14 for **D1**, **CC**, and **MR**, respectively.

3 Results and discussion

In this section, the results pertaining to Proper Orthogonal Decomposition and Dynamic Mode Decomposition on snow particle wake flow characteristics are presented and discussed. Initially, we focus on the POD analysis performed onto data sets ***S1*** and ***S2***, sampled at rate Δt_1. Subsequently, we explore the DMD results from data sets ***S1*** and ***S3***, as explained in Section 2.4, using both sampling rates Δt_1 and Δt_2.

3.1 Wake flow structures past snow particles

To better understand and contextualize the results, we first describe the snow particle falling behavior, as observed during the experiments described in Section 2.1. The dendrite crystal **D1** (Figure A1(a) in the Supplementary Material) displayed stable falling motion for the tested Reynolds number range ($10 \lesssim Re \lesssim 1500$), maintaining its largest projected area orthogonal to the falling direction (Figure A1(a)). **MR**'s stable falling persisted until $Re \approx 250$. Beyond $Re \approx 250$ a falling motion with randomly varying orientations (Figure A1(c)) was noted, which we will refer to as *chaotic* (McCorquodale and Westbrook, 2020b). **CC** exhibited stable falling for $Re \lesssim 70$, transitioning to a mildly spiraling trajectory for $70 \lesssim Re \lesssim 400$, and a spiraling trajectory with more abrupt changes in the orientation for $Re \gtrsim 400$ (Figure A1(b)).

In one of our former studies, we analyzed the wake flow configuration of the presented snowflake geometries (Tagliavini et al., 2021b) and we highlight below the main features in the wake flow for particle **D1**, **CC**, and **MR** at $Re = 1500$ to help in the comprehension of the results. **D1**'s wake flow field displays a small recirculation zone attached to the center of the particle and small vortices that originate from the branches of the dendrite. The recirculation zone and small vortices are sustained and symmetric, creating a stable descent, thus supporting a steady falling motion. **CC**, at the selected extreme orientation, features an asymmetric pair of vortices shed from the tips of the columnar crystal, which are associated with a marked spiraling fall of the particle. The rosette-like crystal (**MR**) has a more unorganized flow within its wake. This creates large and unstable structures that also influence the random orientations displayed by the particle during its descent.

3.2 Spatial resolution sensitivity of Proper Orthogonal Decomposition

In the first part of our work, we investigate the effects of resampling the original streamwise velocity data (***S1***) onto a coarser spatial grid to mimic a less spatially resolved data set (***S2***), such as those collected during experiments (see Section 2.1). This analysis takes into consideration snow particle **D1** (characterized by a steady falling motion), **CC** and

MR (exhibiting unsteady falling behavior), each inducing distinctive wake flow patterns (see Section 2.1). After performing Proper Orthogonal Decomposition on ***S1*** and ***S2***, we removed the mode representing the averaged flow field from each data set to ensure that the remaining modes represent only the fluctuating part of u_x. To begin with, we examine Figure 1, which illustrates the comparison between ***S1*** and ***S2*** with respect to the cumulative energy evaluated as:

$$\text{Energy}(n)[\%] = \frac{E_c}{E_{tot}} \times 100 = \frac{\Sigma_i^n \mu_i^{POD}}{\Sigma_i^N \mu_i^{POD}} \times 100\,, \tag{25}$$

where n is the n-th mode and N is the total number of modes. For snow particle **D1**, which exhibits a steady falling motion and induces less instabilities within the wake, the disparities between the mode energy content of the POD obtained from the original data and those from the resampled ones are negligible, having 92.35% of the energy represented by 20 modes for data set ***S1*** against 91.52% for ***S2***. Conversely, for particles like **CC** and **MR**, which display unsteady falling trajectories and generate more unstable structures in their wakes, a lower spatial resolution produces a noticeable decrease in the energy content carried by each POD mode, from 76.04% (***S1***) to 73.51% (***S2***) of the energy carried by the first 20 modes for **CC**, and from 72.48% (***S1***) to 68.60% (***S2***) for **MR**.

Thereupon, we turn our attention to the features depicted in Figure 2, 3, and 4, related to the visualization of iso-surface of the first and second POD modes and their spatial signal with regard to particles **D1**, **CC**, and **MR**. The first POD mode represents the most energetic mode and displays the dominant features of the flow, which are generally the largest and most energetic structures, while the second mode pertains to smaller and less energetic structures, which account for secondary flow motion within the wake. For the investigated snowflakes, the relative energy carried by the first and second mode is, respectively, 13.66% and 8.74% for **D1**, 7.31% and 6.08% for **CC**, and 8.23% and 6.42% for **MR**. The spatial signal of each mode is sampled along five lines of 2000 points each (Figure A3 in the Supplementary Material) and then averaged, as described in Section 2.4. With respect to particle **D1** (Figure 2), its branched shape introduces small-scale vortices that are sustained in time and space throughout the entire wake. This reflects in the qualitative representation of the first and second POD modes (Figure 2(a) and (b), respectively). Similarities emerge between structures' shape in both the original (***S1***) and the spatially coarse data set (***S2***). However, the structures in ***S2*** exhibit a greater distortion and bulkiness, in particular for the second mode because smaller structures are more sensitive to spatial resolution. By looking closely to the signal, sampled over the previously mentioned lines (Section 2.4), of these two modes, the spatial PSD computed on the signal for the first mode displays higher amplitudes for ***S1*** as compared to ***S2***, whereas the signal shape is preserved (Figure 2(c)). In contrast, Figure 2(d) shows that the signals of the second mode are in opposite phase. This phase disparity stresses the POD sensitivity to alterations in spatial resolution of the input data that might be noticed due to several factors, such as aliasing effect and resolution-induced phase shift (De Schryver, 2016). High wavenumbers in the spectra (Figure 2(c, d), right side) confirm the presence of small structures which are mildly smeared out by spatial resampling. Shifting our focus towards particle **CC** (Figure 3), the qualitative visualization of the POD modes sheds light upon the large, elongated structures rising from both sides of the particle, which are representative of the vortex street shed from the columnar crystal's tips (Tagliavini et al., 2021b). For this geometry, both the qualitative visualization (Figure 3(a, b)) and the spatial spectral analysis (Figure 3(c, d)) show that for the resampled data ***S2***, POD tends to underestimate the spectral energy variations carried by smaller-scale wake flow structures, while exhibiting peaks in the spectra at high wavenumbers. In fact, the shape of the spectra for ***S1*** and ***S2*** is preserved, but PSD at lower wavenumbers are smeared out from ***S2***. Therefore, the information at lower scales is lost when decreasing the spatial resolution. A similar behavior is found for **MR** (Figure 4(a, b)), also characterized by an unsteady falling motion and strong wake flow instabilities (McCorquodale and Westbrook, 2020b; Tagliavini et al., 2021b). Even in this case, POD carried out on resampled data contains less details regarding the wake flow field. If we take a look at the spatial signals and their FFT (Figure 4(c, d)), this is visible from the discrepancies at low wavenumbers, at which the PSD of ***S2*** is smeared out, as compared to ***S1***.

The structures highlighted by the POD analysis corroborate the observations of the wake flow characteristics and falling behavior from both numerical simulations and experiments (McCorquodale and Westbrook, 2020b; Tagliavini et al., 2021b). Furthermore, the results stress the impact of spatial resolution on POD. In cases where the flow is characterized by small, uniformly distributed structures, as for **D1**, the impact of spatial resolution is limited. On the contrary, with flows where large structures are present (**CC**, **MR**), a lower spatial resolution can affect the information that the POD is able to capture. These findings are valuable when dealing with experiments characterized by low spatial resolution. They suggest that despite spatial limitations, essential flow features remain captured, when the flow exhibits more organized patterns. However, in cases of stronger wake flow instabilities, it is essential to exercise caution when interpreting smaller scale structures, as these might be smeared out or distorted.

3.3 Dynamic Mode Decomposition on flow data with and without force contribution

With Dynamic Mode Decomposition, by considering the linearization of a non-linear system, we do not obtain modes representing the energetically dominant flow dynamics, as with Proper Orthogonal Decomposition, but we identify modes that evolve in time and space, and can therefore capture transient and non-periodic features of the flow field. The resulting eigenvalues are complex conjugate pairs that describe the temporal behavior, while the modes carry the information about the spatial features of the flow. For this purpose, the goal of this second part is to investigate the sensitivity of DMD to temporal resolution and to the inclusion of the information related to the forces acting on the particle into the snapshot matrix. In this view, both sampling rates Δt_1 (1000 Hz) and Δt_2 (500 Hz) are considered and the analysis is performed on two different snapshot matrices: the first one derived from the streamwise velocity field of the numerical model (***S1***) and the second one created by adding the forces exerted on each particle in the x, y, and z direction (***S3***) to the original snapshot matrix, as described in Section 2.4. Before performing the comparison, all the resulting modes are sorted according to the energy criterion from Equation (20). In this way, the modes are selected according to their energy content. Furthermore, the mode corresponding to the average u_x field is removed from the DMD results to ensure that only transient features are considered.

3.3.1 DMD temporal dynamics

We initially focus on the temporal part of the signal, considering the first 100 DMD modes, as reconstructed from Equation (22). The PSD of $\boldsymbol{X}_{\text{rec}}^{DMD}(t)$ is evaluated using Equation (23) for both data sets ***S1*** and ***S3***, at two different sampling rates Δt_1 and Δt_2. This comparison is depicted in Figure 5 (left side: ***S1***, right side: ***S3***), which also includes the power spectral densities from the temporal evolution of the forces acting on the snowflakes in x, y, and z directions, directly calculated from the numerical model. The forces spectra exhibit increasing fluctuation as we move from a steady falling motion (**D1**, Figure 5(a)) to more convoluted fall trajectories (**CC** and **MR**, Figure 5(b, c)). By looking at the spectra of the reconstructed temporal signals, we notice that the sampling rate has a strong impact on the energy content, especially for the particles with strong wake instabilities (**MR**, **CC**). The use of the sampling rate Δt_2 seems to neglect important temporal features in both data sets and shows a lower energy content. This loss becomes more pronounced when stronger unsteadiness, such as vortex shedding (as observed by Tagliavini et al. (2021b)), comes into play (**CC** and **MR**). Therefore, the choice of the sampling frequency appears to be decisive for the accuracy of the temporal part in the DMD analysis of the wake flow. On the right-hand side of Figure 5, the reconstructed signals from data set ***S3*** present a comparable trend to those of the forces exerted on the particles, meaning that the counting of the forces inside the snapshot matrix appears to have a mitigating effect on the loss of information for lower sampling rates (Δt_2). This improvement can be seen from the high energy content of the orange and green curves on the right-hand side of Figure 5(c, d) for particle **CC** and **MR**, respectively, as compared to the plots on the left. The presence of a peak in the PSD for the lower sampling rate Δt_2 in the **MR** case (Figure 5(d), left-hand side, green curve) could be due to aliasing or insufficient resolution to capture the high-frequency dynamics correctly: unsteady motions involve a broad spectrum of frequencies, and a lower sampling rate might fail to resolve some of these frequencies, leading to artifacts or spurious peaks in the spectrum (De Schryver, 2016). The influence of temporal resolution and the inclusion of forces in the snapshot matrix is also visible from the exponential eigenvalues λ_i^{DMD} plotted onto the complex plane, as reported in Figure A4 and A5 of the Supplementary Material.

The motivation for comparing the FFTs of reconstructed signals from the streamwise velocity field alone (***S1***) and combined with temporal force signals (***S3***) to the PSD of forces acting on the particle lies in understanding the complex interplay between flow dynamics and force dynamics. The first aspect to consider is the force-flow-snowflake motion interaction, wherein the forces acting on the particle are a direct manifestation of the underlying wake flow structures. By incorporating the force data into the snapshot matrix of the streamwise velocity, we are able to capture this forces- wake flow structures-snowflake falling motion interaction more effectively. In addition, forces often include high-frequency components, resulting from rapid changes in the flow around the unstably falling particle. Incorporating these into the DMD analysis helps in capturing these high-frequency dynamics that might be missed when using only the velocity field data.

3.3.2 DMD spatial dynamics

We now look at the spatial characteristics of the DMD modes, particularly evaluating the spatial power spectral density derived through Fast Fourier Transform (Equation (19)). Employing only Δt_1 as the sampling rate, we concentrate on the first four DMD modes, selected according to the criterion given in Equation (20). We sample the streamwise velocity field u_x in the wake along five distinct lines (Figure A3 in the Supplementary Material), as detailed in Section 2.4. After that, the signal along each of these sampling lines is averaged and the spatial FFT is then performed. Figures 6, 7, and 8 depict the results for the first two modes, for particle **D1**, **CC**, and **MR**, respectively, whereas the data related to the third and fourth mode can be found in Figure A6, A7, and A8 of the Supplementary Material.

By looking at the visual representations of the iso-surfaces from the first two modes of **D1** (Figure 6(a, b)), we observe red and blue zones that indicate coherent structures of opposed directions, with slight variations in the shape and intensity in the case the particle forces are included (***S3***). The wake flow structures appear of small scale and are sustained through the entire length of the wake, which can be directly linked to the stable falling motion of the dendrite-like particle (Tagliavini et al., 2021b). Regarding particle **CC** (Figure 7(a, b)), both the first and the second DMD mode present more pronounced structures with marginally more intricate patterns for data set ***S3***. For both ***S1*** and ***S3***, the flow tends to separate laterally at the column caps where structures of opposite directions (red and blue) are generated, indicating the presence of shed vortices (Tagliavini et al., 2021b) which influence the spiraling fall of the particle (McCorquodale and Westbrook, 2020b). The rosette-like snowflake (**MR**, Figure 8(a, b)) exhibits large, randomly distributed coherent structures. This disorganized distribution is consistent with the wake flow features and *chaotic* fall trajectories observed for the **MR** geometry in former studies (McCorquodale and Westbrook, 2020b; Tagliavini et al., 2021b).

A more quantitative analysis can be found in Figure 6(c, d), in which the averaged spatial signal of the two modes and the respective wavenumber spectra are shown for the dendrite-like particle (**D1**). While the comparison between the power spectral densities of the first mode exhibit more distinct and higher spatial variations for ***S3***, the differences between such curves become less significant for the second mode. The inclusion of the forces provides additional information about the flow dynamics, by informing the linear operator $\boldsymbol{A}$ in the DMD of variations near the snowflake influencing the force distribution around it as well as its falling motion. For particles characterized by small and non-persistent instabilities within the wake flow, such as the **D1** case, this might result in a spectrum with higher energy content, when forces are included in the snapshot matrix, and more marked peaks at high wavenumbers. This phenomenon is less visible for particle **CC** and **MR** (Figure 7(c, d) and 8(c, d), respectively). These two particle manifest larger structures in their wakes, which are less affected by the inclusion of the forces. When considering the spatial characteristics, other factors need to be taken into account. First of all, spatial averaging comes into play when the signal is sampled along the wake, effectively mitigating the influence of local fluctuations or noise in the data, resulting in a smoother spatial signal. This effect is less strong when the flow field exhibits small-scale and intermittent instabilities (**D1**) because of the presence of more compact, organized main flow structures. Besides, while temporal variations in flow data can be highly sensitive to transient effects of the forces acting on the particle (Figure 5), spatial analysis focus on spatial coherence of the flow structures, making the inclusion of the forces less critical.

To summarize, the differences in spatial signals between data sets ***S1*** and ***S3*** are more pronounced for particle **D1**, characterized by reduced unsteadiness within its wake flow, in contrast to **MR** and **CC**, which exhibit unorganized flow patterns, leading to a wide range of spatial scales.

3.3.3 Wake flow characteristics and particle shape features

In the final part of this work, we look at the relation between the snow particle shape descriptors, the spatial and the temporal information obtained from DMD. For this purpose, we focus on Figure 9 and 10 which relate the minimum and maximum DMD eigenfrequency, the maximum and minimum DMD absolute growth or decay rate, and the maximum and minimum wavenumber from the PSD of the line-averaged first DMD mode, respectively, to the shape porosity of each particle (Equation (24) in Section 2.4).

As previously mentioned, Figure 9 shows the DMD eigenfrequencies (γ_{min}^{DMD} in Figure 9(a), and γ_{max}^{DMD} in Figure 9(b)) for data sets ***S1*** and ***S3***. These values are compared with the snowflake shape porosity ϵ. High values of ϵ imply small particle frontal area with respect to an enclosing disk, which promote the reduction of flow separation and vortex shedding, as observed by Cummins et al. (2018) and Tagliavini et al. (2021b). This is clear also from the eigenfrequency values of **D1** which are the lowest for both ***S1*** and ***S3***, indicating the presence of less oscillating structures. As opposed to **D1**, **CC** and **MR** display higher γ_{min}^{DMD} and γ_{max}^{DMD} with **MR** exhibiting the highest values, in agreement with its increasing oscillations in the wake flow and its *chaotic* fall trajectory. A linear trend is observed for both data sets and can be attributed to the relation between shape porosity and its immediate effect on the flow dynamics around the particle, which affect the DMD eigenfrequencies. ***S3*** presents a steeper linear profile than ***S1*** for the minimum frequency (Figure 9(a)). The linear relationship between minimum eigenfrequency and porosity is stronger when forces are included in the snapshot matrix, as highlighted by the higher values of the coefficient of determination R^2, and suggests a significant sensitivity of γ_{min}^{DMD} with respect to ϵ. Regarding γ_{max}^{DMD}, a less perceptible difference in the linear profile steepness between ***S1*** and ***S3*** demonstrates that the accounting for the forces influences the low eigenfrequencies more than the high ones. This can be explained by the fact that low eigenfrequencies correspond to less oscillating structures within the wake flow, which might be enhanced by the inclusion of the forces due to their temporal nature (see Section 3.3.1). Furthermore, the forces acting on the particle influence the long-term dynamics of the flow, which is why their inclusion in the DMD analysis tends to reflect on lower frequencies more significantly. An overall improvement in the linear trends appear whenever the forces are taken into account in the DMD analysis. Figure 9(c, d) illustrates the comparison between porosity ϵ and the minimum and maximum absolute decay or growth rate from DMD ($\Re(\lambda_i^{DMD}) = \sigma_i$) for all the three snow particles, for which a linear relationship is also established. High porosity particles, such as **D1**, exhibit strongly decaying ($\Re(\lambda_i^{DMD})_{min}$) or stable ($\Re(\lambda_i^{DMD})_{max}$) wake flow structures, resulting in more steady falling trajectories (McCorquodale and Westbrook, 2020b; Tagliavini et al., 2021b). Conversely, low-porosity particles, such as **CC** and **MR**, generate mildly decaying ($\Re(\lambda_i^{DMD})_{min}$) or growing structures ($\Re(\lambda_i^{DMD})_{max}$), leading to strong unsteadiness within the wake flow, thus more complex falling trajectories (McCorquodale and Westbrook, 2020b). The inclusion of forces acting on the snowflake in the snapshot matrix enhances our understanding of the interdependence between snowflake shape, wake flow features, and particle falling behavior. This effect is particularly evident in Figure 9(d), where high $\Re(\lambda_i^{DMD})_{max}$ values correspond to large wake flow instabilities and unsteady falling trajectories, as observed for **MR**. These findings establish a quantitative link between particle shape and wake flow characteristics, provide a method to predict wake flow instability and falling behavior based on particle geometrical features, and highlight the importance of considering both shape and forces in understanding snowflake dynamics.

Afterwards, we correlate the snowflake shape porosity to the minimum and maximum wavenumber from the spatial FFT of the first DMD mode (Equation (19) using $\overline{\Phi^{DMD}}$), adimensionalized with the particle maximum dimension: $\kappa^*_{min} = D_{max} \cdot \kappa_{min}$ and $\kappa^*_{max} = D_{max} \cdot \kappa_{max}$ (with D_{max} the particle's maximum extension orthogonal to the flow direction, Figure 10(a, b)). The first mode is selected because it is the most energetic one (according to the selection criterion of Equation (20)) and generally carries the majority of the information on the flow dynamics. Similarly to the eigenfrequencies, the PSD wavenumbers also manifest a linear trend with respect to the shape porosity for both ***S1*** and ***S3***, and from the coefficient of determination (R^2) values reported in Figure 10, a slightly better agreement for data ***S3*** can be seen. However, no significant change in the slope between ***S1*** and ***S3*** is visible in Figure 10. In analogy of what we previously seen in Figure 6, 7, and 8, with respect to the spatial signals, the inclusion of the forces in the snapshot matrix does not significantly impact the spatial information. The linear relationship indicates that shape porosity plays a crucial role, not only in the temporal, but also in the spatial dynamics of the wake flow, influencing the size of the coherent structures that forms within the wake and thus impacting the particle falling motion, as discussed by Köbschal et al. (2023) and Sánchez-Rodríguez and Gallaire (2024). The highly porous shape of **D1** (steady falling behavior) allows more fluid to pass through its structure, creating organized, finer-scale structures, which reflect onto higher wavenumbers. The intermediate porosity of **CC** (spiraling fall trajectory (McCorquodale and Westbrook, 2020b)) generates moderate complexity within the wake flow. This results in alternating small- and large-scale structures that correspond to intermediate values for the maximum and minimum wavenumbers. The least porous shape (**MR**, *chaotic* falling motion (Section 3.1)) displays large-scale wake flow structures, which find correspondence in low wavenumbers. For all the examined cases, the wavenumber from the spatially averaged spectra increases with increasing porosity. This denotes that a more porous geometry likely creates small-scale and intermittent structures within the wake flow that directly affect the falling trajectory of the particle, making it more stable (**D1**) (Cummins et al., 2018; Tagliavini et al., 2021b), while more porous shapes (low shape porosity) promote medium- and large-scale, temporally unstable structures that give rise to oscillating or *chaotic* falling behavior (**CC**, **MR**).

4 Conclusions

This study employed Proper Orthogonal Decomposition (POD) and Dynamic Mode Decomposition (DMD) to investigate the wake flow structures of three distinct snowflake geometries: a dendrite crystal (**D1**), a columnar crystal (**CC**), and a rosette-like crystal (**MR**). Our comprehensive analysis has yielded significant insights into the complex relationships between snowflake shape, wake flow characteristics, and falling behavior.

POD revealed that spatial resolution sensitivity depends on the type of structures within the snow particle wake. For particles with steady falling motions (**D1**), the wake flow displayed small, organized structures and the impact of spatial resolution was minimal. However, for particles with more complex wake flow (**CC** and **MR**), where larger structures are present, lower spatial resolution affected the information that the POD was able to capture at lower wavenumbers. This finding underscores the importance of spatial resolution considerations in experimental data interpretation, particularly for particles with complex wake flow.

DMD provided crucial insights into both temporal and spatial dynamics of snowflake wake flows. We found that temporal resolution significantly affects how well the reconstructed temporal spectra from DMD match the forces' spectra, especially for particles with strong wake flow instabilities. Including particle forces in the snapshot matrix improved the representation of high-frequency dynamics and mitigated information loss at lower sampling rates, particularly for particles with unsteady falling motions. Spatially, the DMD analysis showed distinct wake flow structures for each particle geometry. **D1** exhibited small-scale structures, consistent with its stable falling motion. **CC** showed lateral flow separation at the column caps, with larger structures with marginally more intricate patterns. **MR** displayed randomly distributed large, coherent structures, aligning with its *chaotic* fall trajectory. The inclusion of forces in the snapshot matrix had a less decisive effect on the spatial dynamics, as compared to its effect on temporal dynamics, producing a slight increase in the spectral energy content for the case of particle **D1**.

A key contribution of this study is the establishment of quantitative links between particle shape (characterized by shape porosity), wake flow characteristics, and snow particle falling motion. We observed linear trends between particle porosity and the extracted DMD parameters, i.e. eigenfrequencies, growth or decay rates, and wavenumbers. High-porosity particles (**D1**) exhibited more stable, small-scale flow structures in the wake, corresponding to steady falling behavior, while low-porosity particles (**CC** and **MR**) generated larger, less stable structures associated with more complex falling trajectories. The inclusion of force data stressed the complex interplay between snowflake shape, wake flow features, and particle falling behavior, offering a more complete understanding of snowflake aerodynamics.

This study has significantly advanced our understanding of the wake flow of complex-shaped snow particles, providing both theoretical insights and practical tools for predicting snowflake falling behavior. Future work could extend this analysis to a broader range of snowflake geometries to further elucidate the relationships between particle shape, wake flow characteristics, and falling trajectories, which will allow for more accurate and reliable snow precipitation models, with far-reaching implications for weather forecast.

Authors' contribution

Giorgia Tagliavini: conceptualization; data curation; formal analysis; investigation; methodology; software; visualization; writing of the original draft.

Markus Holzner: reviewing and editing of the final draft; partial funding.

Pascal Corso: conceptualization; formal analysis; investigation; methodology; reviewing and editing of the drafts; software; supervision.

Acknowledgements

The numerical simulations were performed using ETH - Euler cluster resources of *Prof. Dr. Roman Stocker*'s Group from the Department of Civil, Environmental and Geomatic Engineering at ETH Zürich. The modal analysis calculation was supported by the computing resources from the Swiss National Supercomputing Centre (CSCS) under project ID s1210 of *Dr. Pascal Corso.*

The authors would like to thank *Prof. Dr. Peter Schmid* for the insightful discussion about incorporating forces data in the Dynamic Mode Decomposition matrix and *Nebojsa Dubocanin* for his preliminary work on the code related to modal analysis on 2D numerical data which was improved and extended to produce the results presented in this manuscript.

Last but not least, the authors would like to thank *Dr. Mark McCorquodale* and *Dr. Chris Westbrook* for sharing the experimental data, which provided crucial information for the validation of the numerical model and the interpretation of the results of the current article.

Conflict of interest

The authors declare to have no conflict of interest.

Data and materials availability

The data that support the findings of this study are available from the corresponding author upon reasonable request.

Tables and figures

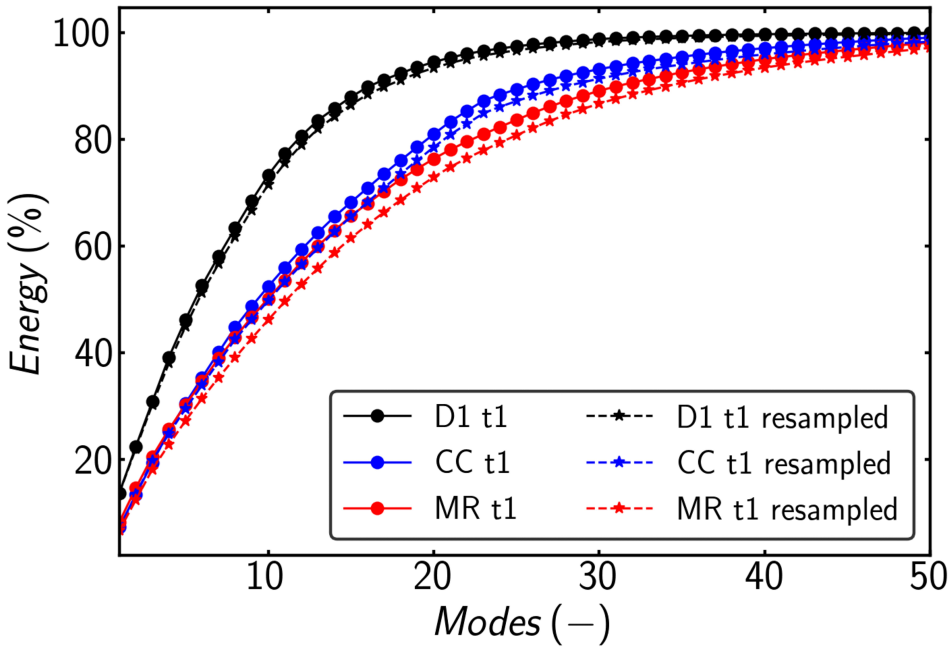

Figure 1: Cumulative energy percentage carried by each mode extracted from POD (Equation (25)) with the highest sampling frequency (Δt_1). The comparison is made between the original (***S1***) and the resampled numerical data (***S2***), as explained in Section 2.4.

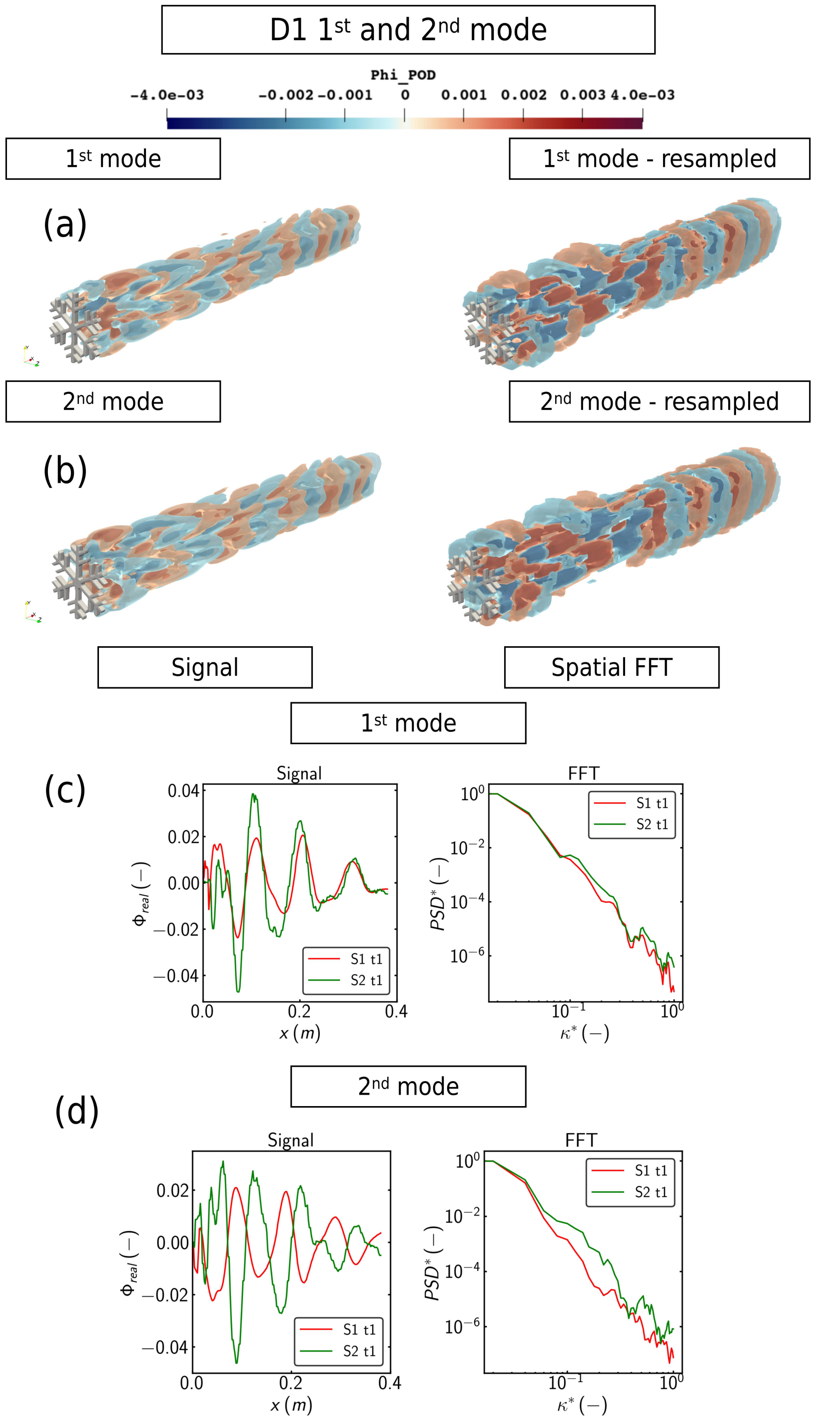

Figure 2: First and second mode resulting from Proper Orthogonal Decomposition performed on the numerical (left) and the resampled data sets (right), respectively, pertaining to particle **D1**. The top part of the figure qualitatively illustrates the spatial distribution of the first (a) and the second (b) mode, while the bottom part shows the quantitative comparison between the spatial signals and their power spectral density of ***S1*** and ***S2*** for the first (c) and second (b) POD mode. The power spectral density and wavenumber are normalized using their maximum values $\mathrm{PSD}^* = \mathrm{PSD}/\mathrm{PSD}_{max}$ and $\kappa^* = \kappa/\kappa_{max}$ (see Section 2.4).

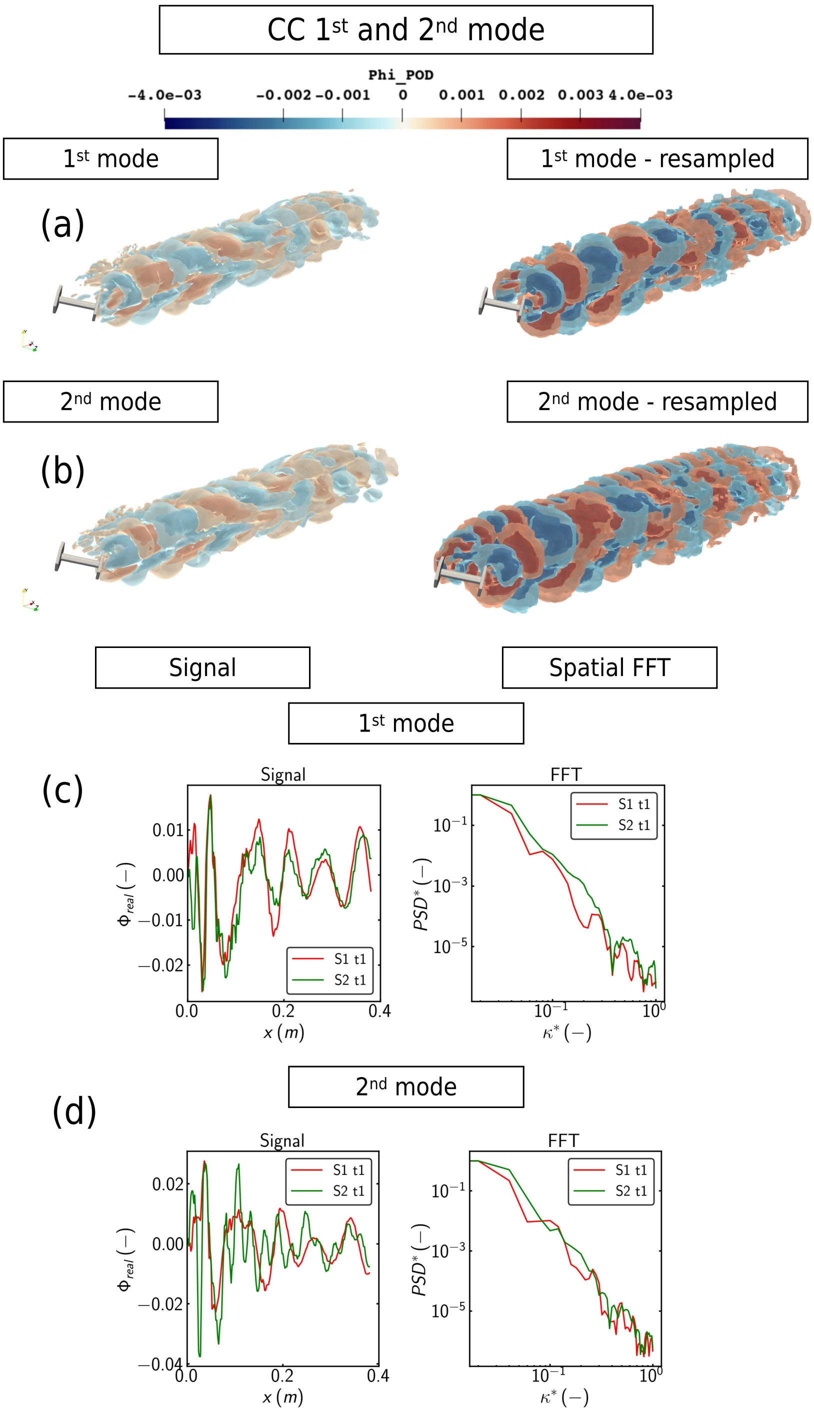

Figure 3: First and second mode resulting from Proper Orthogonal Decomposition performed on the numerical (left) and the resampled data sets (right), respectively, pertaining to particle **CC**. The top part of the figure qualitatively illustrates the spatial distribution of the first (a) and the second (b) mode, while the bottom part shows the quantitative comparison between the spatial signals and their power spectral density of ***S1*** and ***S2*** for the first (c) and second (b) POD mode. The power spectral density and wavenumber are normalized using their maximum values $\mathrm{PSD}^* = \mathrm{PSD}/\mathrm{PSD}_{max}$ and $\kappa^* = \kappa/\kappa_{max}$ (see Section 2.4).

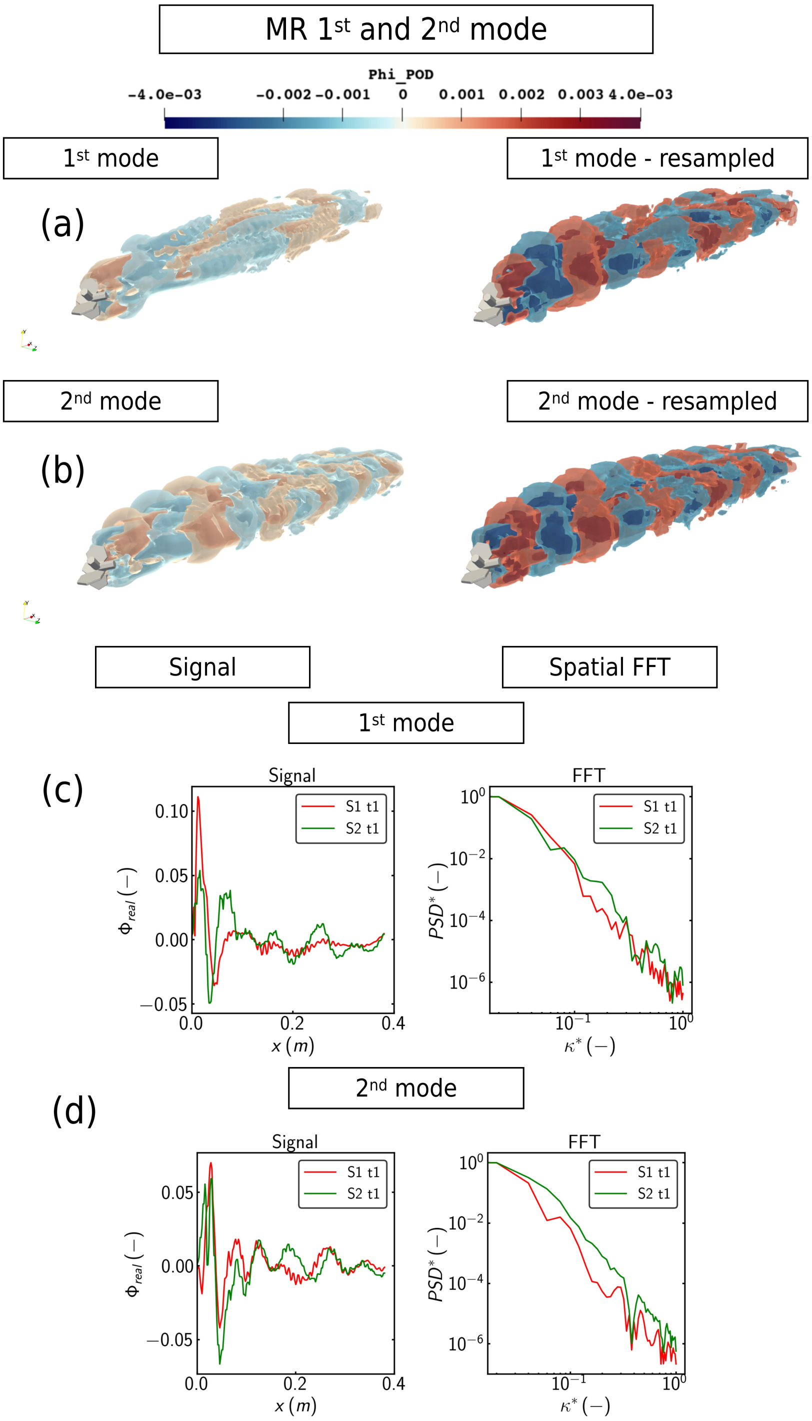

Figure 4: First and second mode resulting from Proper Orthogonal Decomposition performed on the numerical (left) and the resampled data sets (right), respectively, pertaining to particle **MR**. The top part of the figure qualitatively illustrates the spatial distribution of the first (a) and the second (b) mode, while the bottom part shows the quantitative comparison between the spatial signals and their power spectral density of ***S1*** and ***S2*** for the first (c) and second (b) POD mode. The power spectral density and wavenumber are normalized using their maximum values $\mathrm{PSD}^* = \mathrm{PSD}/\mathrm{PSD}_{max}$ and $\kappa^* = \kappa/\kappa_{max}$ (see Section 2.4).

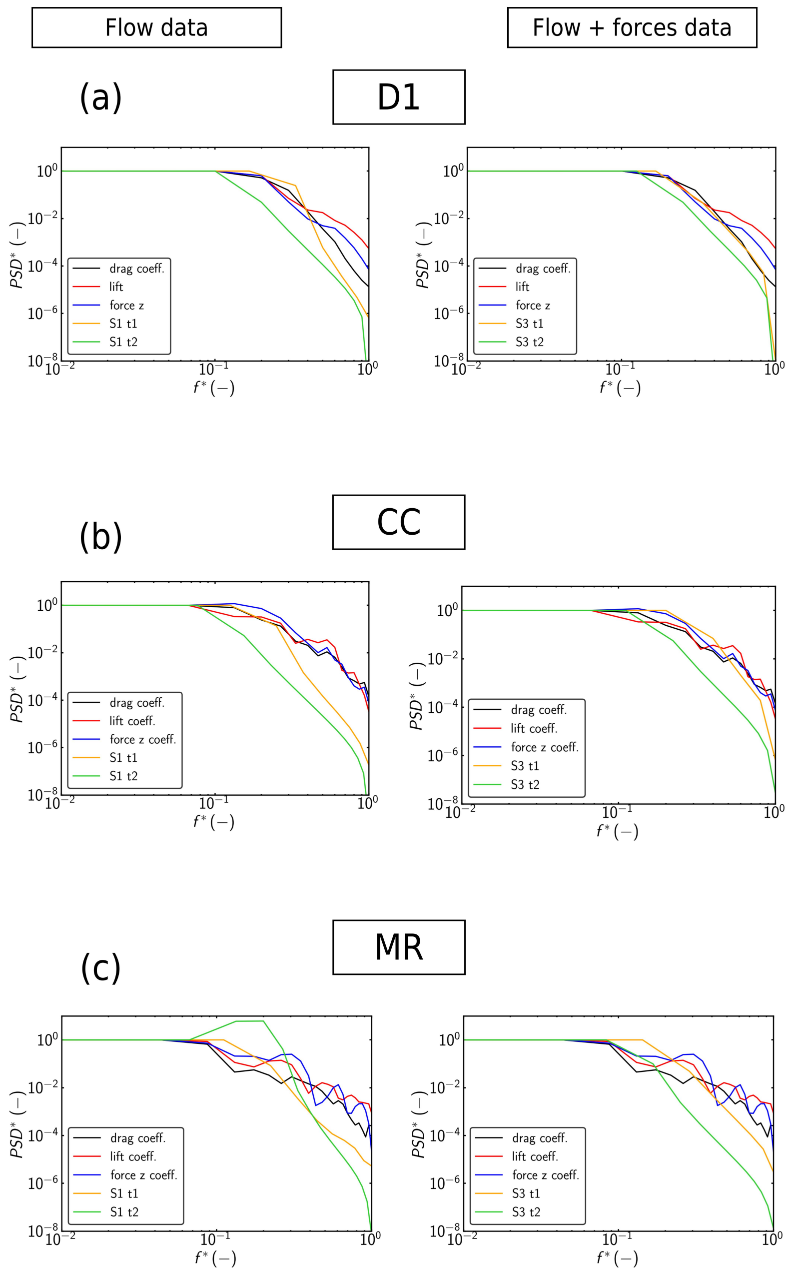

Figure 5: Comparison of the power spectra for all the three snowflake geometries **D1** (a), **CC** (b), and **MR** (c). The reconstructed temporal signal (see Equation (22)) of the first 100 DMD modes, of data sets ***S1*** and ***S3*** and for both sampling rates Δt_1 and Δt_2, is compared with the temporal signal of the forces acting on each particle in x (drag), y, and z (lift components) direction. On the left side the data of the numerical flow field are presented, whereas on the right those including the forces acting on the particles are shown. The power spectral density and frequency are normalized with their maximum values $\text{PSD}^* = \text{PSD}/\text{PSD}_{max}$ and $f^* = f/f_{max}$ (see Section 2.4).

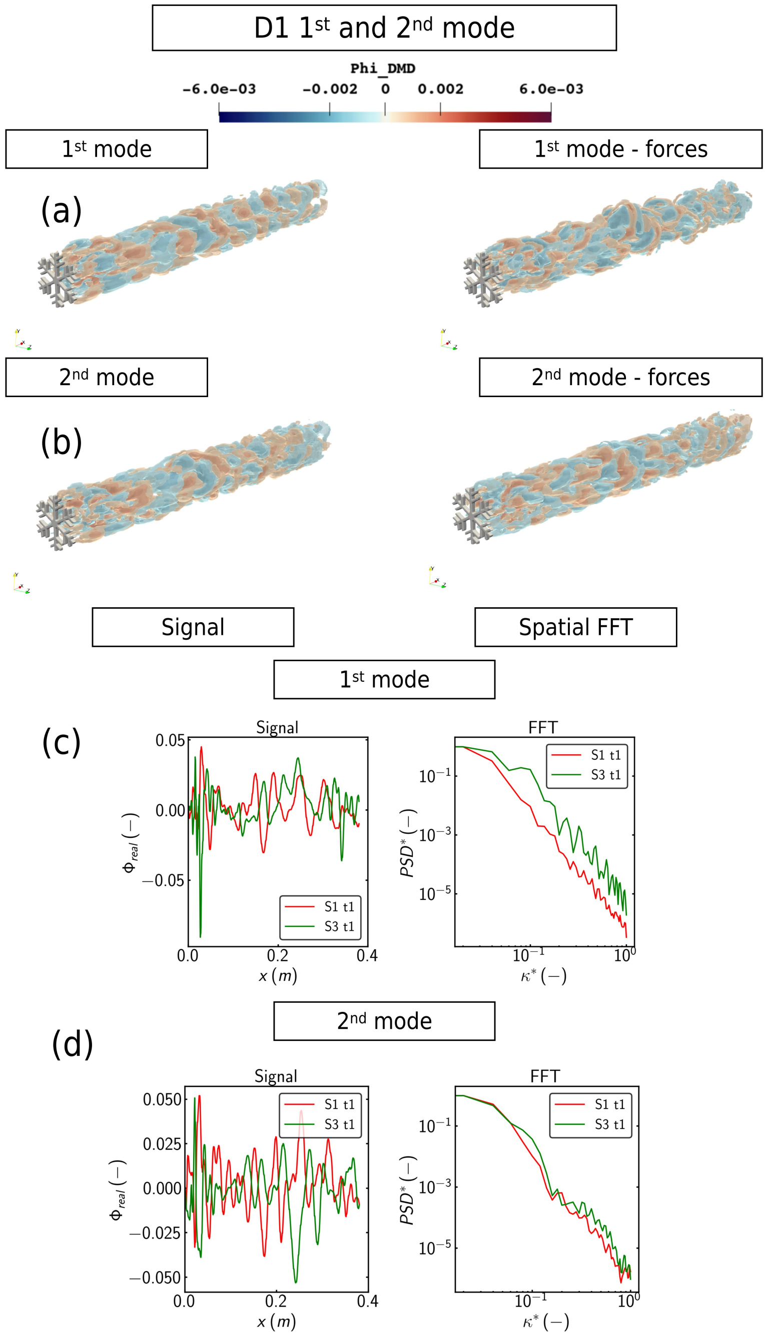

Figure 6: First and second mode resulting from Dynamic Mode Decomposition performed on the numerical data (left) and the numerical data with the forces included in the snapshot matrix (right), pertaining to particle **D1**. The top part of the figure qualitatively illustrates the spatial distribution of the first (a) and the second (b) mode, while the bottom part shows the quantitative comparison between the spatial signals and their power spectral density of ***S1*** and ***S3*** for the first (c) and second (b) DMD mode. The power spectral density and wavenumber are normalized with their maximum values $\mathrm{PSD}^* = \mathrm{PSD}/\mathrm{PSD}_{max}$ and $\kappa^* = \kappa/\kappa_{max}$ (see Section 2.4).

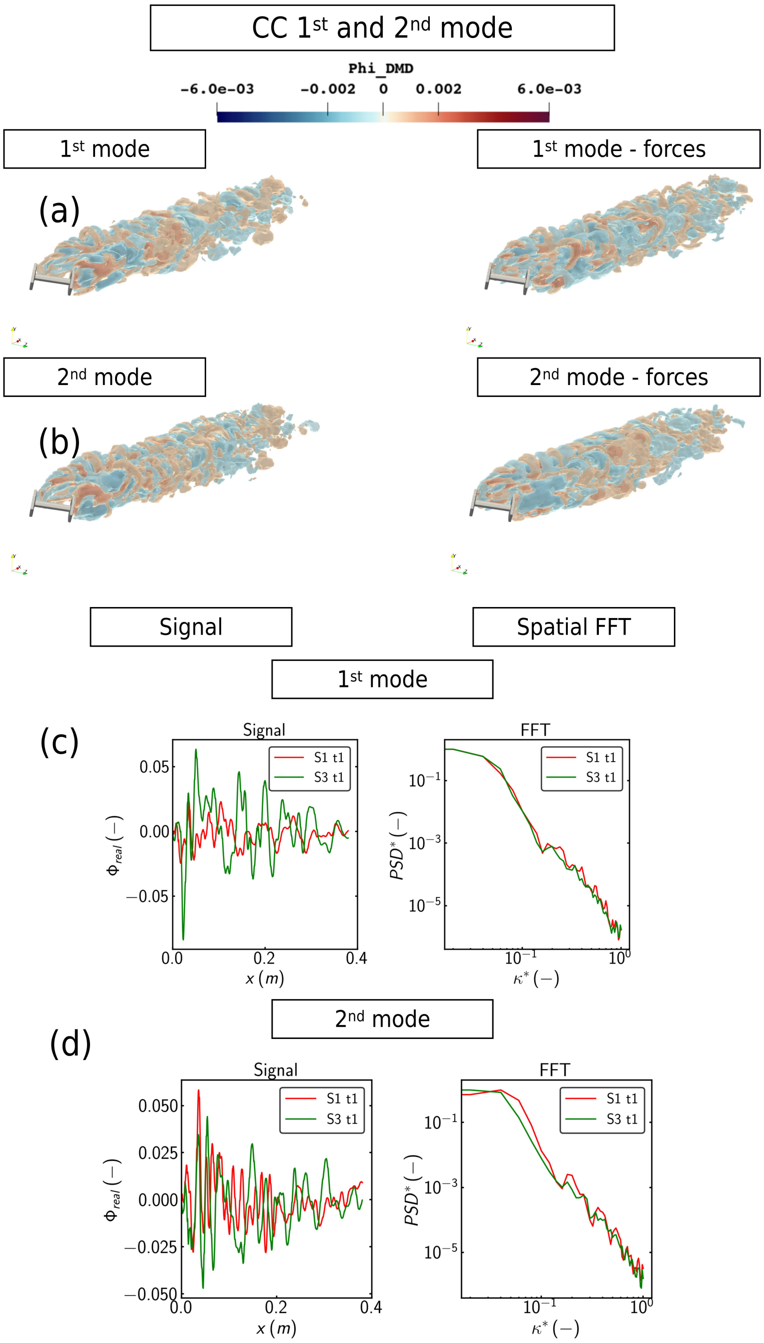

Figure 7: First and second mode resulting from Dynamic Mode Decomposition performed on the numerical data (left) and the numerical data with the forces included in the snapshot matrix (right), pertaining to particle **CC**. The top part of the figure qualitatively illustrates the spatial distribution of the first (a) and the second (b) mode, while the bottom part shows the quantitative comparison between the spatial signals and their power spectral density of ***S1*** and ***S3*** for the first (c) and second (b) DMD mode. The power spectral density and wavenumber are normalized with their maximum values $\mathrm{PSD}^* = \mathrm{PSD}/\mathrm{PSD}_{max}$ and $\kappa^* = \kappa/\kappa_{max}$ (see Section 2.4).

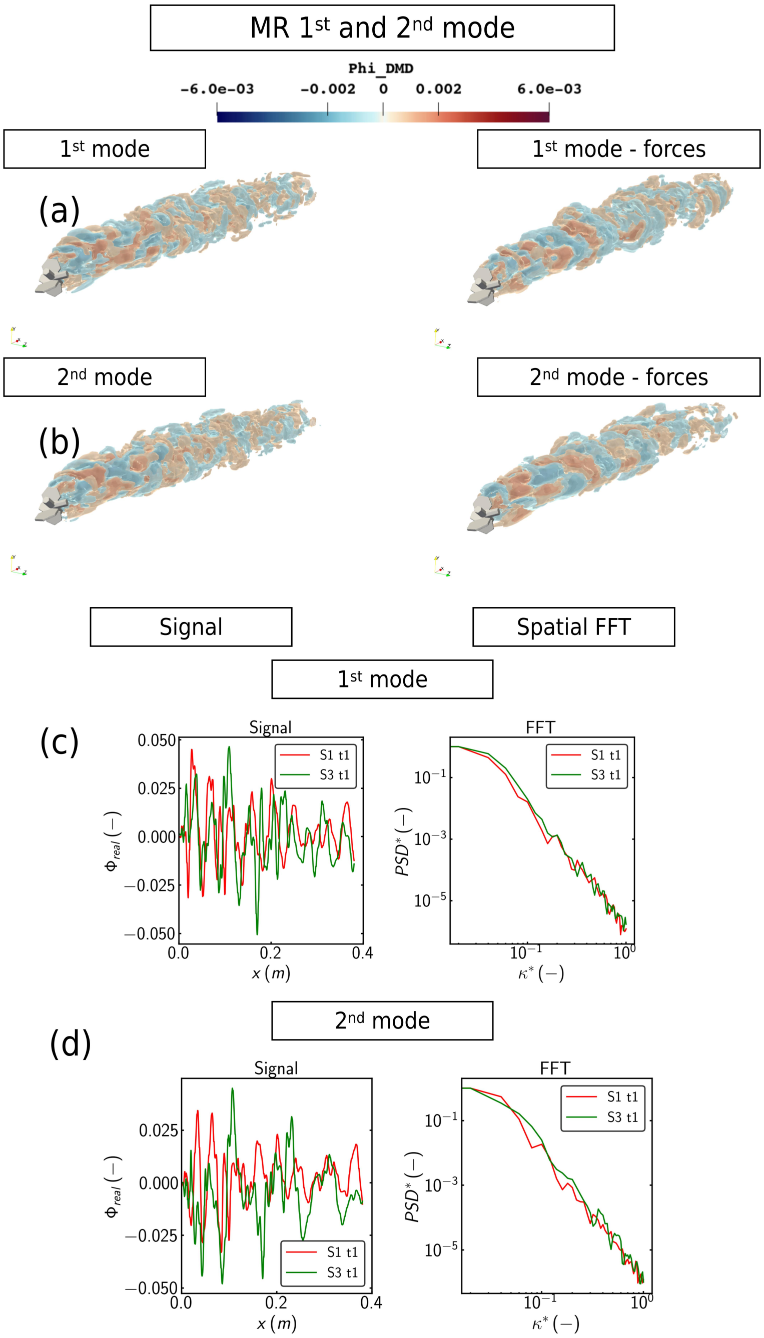

Figure 8: First and second mode resulting from Dynamic Mode Decomposition performed on the numerical data (left) and the numerical data with the forces included in the snapshot matrix (right), pertaining to particle **MR**. The top part of the figure qualitatively illustrates the spatial distribution of the first (a) and the second (b) mode, while the bottom part shows the quantitative comparison between the spatial signals and their power spectral density of ***S1*** and ***S3*** for the first (c) and second (b) DMD mode. The power spectral density and wavenumber are normalized with their maximum values $\text{PSD}^* = \text{PSD}/\text{PSD}_{max}$ and $\kappa^* = \kappa/\kappa_{max}$ (see Section 2.4).

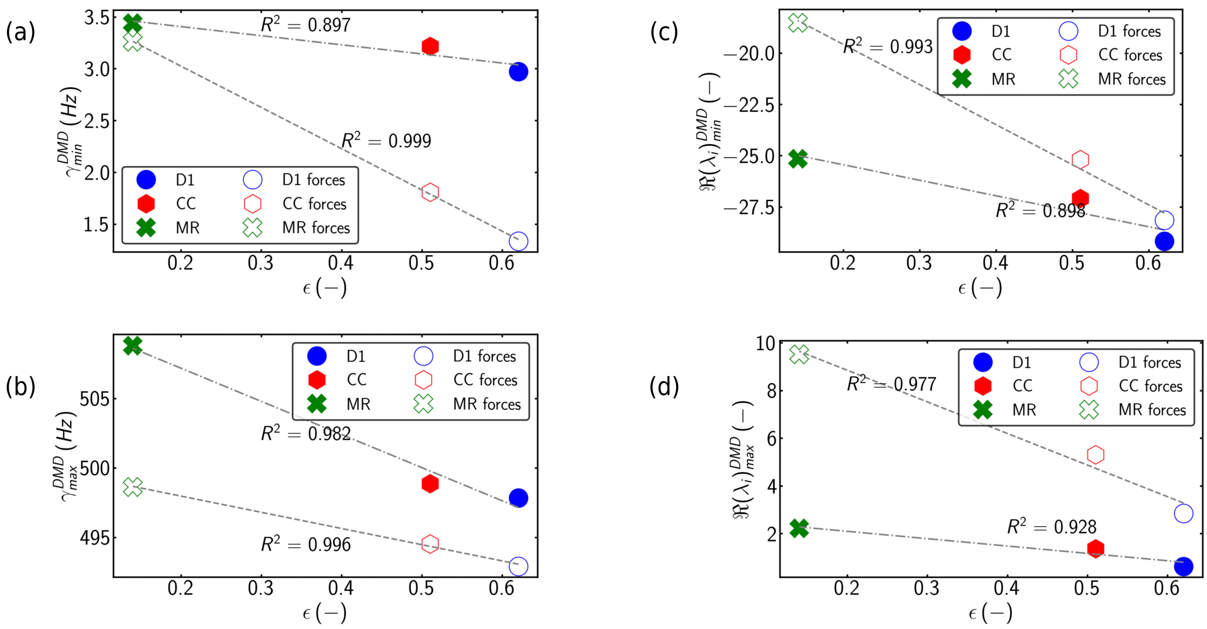

Figure 9: Relation between shape porosity (Equation (24)) and the minimum γ_{min}^{DMD} (a) and maximum γ_{max}^{DMD} (b) DMD eigenfrequencies and minimum $\Re(\lambda_i^{DMD})_{min}$ (c) and maximum $\Re(\lambda_i^{DMD})_{max}$ (d) absolute decay or growth rate of the first 100 DMD modes for each snow particle geometry (Section 2.4). The full symbols represent the numerical data sets, while the hollow markers refer to the numerical data with the forces added in the snapshot matrix. A trend line is also shown together with the quality of the fitting (R^2) to highlight the improvements obtained when the forces are taken into account. For the slope value of each trend line, see Table A1 in the Supplementary Material.

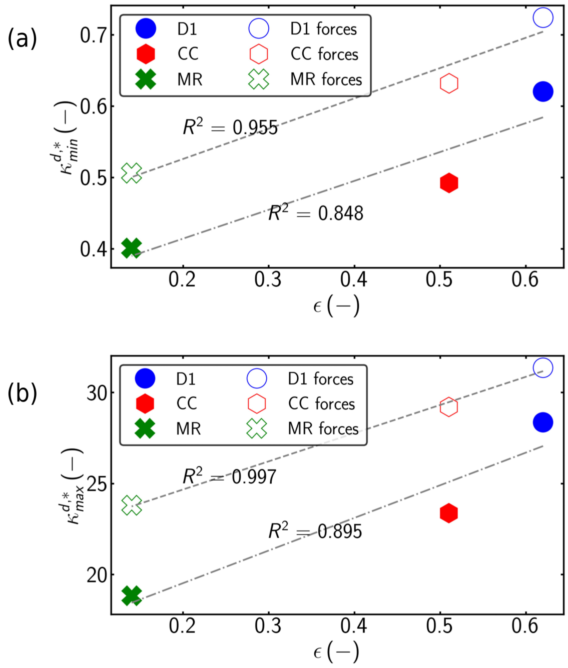

Figure 10: Relation between shape porosity (Equation (24)) and the minimum $\kappa^{d,*}_{DMD,min}$ (a) and maximum $\kappa^{d,*}_{DMD,max}$ (b) wavenumber of the averaged spatial signal of the first DMD mode for each snow particle geometry (Section 2.4). The first mode is selected because it is the most energetic one and generally carries the majority of the information regarding the wake flow structures. The full symbols represent the numerical data sets, while the hollow markers refer to the numerical data with the forces added in the snapshot matrix. A trend line is also shown together with the quality of the fitting (R^2) to highlight the improvements obtained when the forces are taken into account. For the slope value of each trend line, see Table A1 in the Supplementary Material.

References

R. J. Adrian. Particle-imaging techniques for experimental fluid mechanics. *Annual Review of Fluid Mechanics*, 23(1):261–304, 1991.

F. Aguirre, J. Carrasco, T. Sauter, C. Schneider, K. Gaete, E. Garín, R. Adaros, N. Butorovic, R. Jaña, and G. Casassa. Snow cover change as a climate indicator in brunswick peninsula, patagonia. *Frontiers in Earth Science*, 6, 2018.

F. Auguste, J. Magnaudet, and D. Fabre. Falling styles of disks. *Journal of Fluid Mechanics*, 719:388–405, 2013.

M. P. Bailey and J. Hallett. A comprehensive habit diagram for atmospheric ice crystals: Confirmation from the laboratory, airs ii, and other field studies. *Journal of the Atmospheric Sciences*, 66(9):2888 – 2899, 2009.

B. A. Belson, J. H. Tu, and C. W. Rowley. Algorithm 945: Modred—a parallelized model reduction library. 40(4), 2014. ISSN 0098-3500.

E. Bender, M. Lehning, and J. Fiddes. Changes in climatology, snow cover, and ground temperatures at high alpine locations. *Frontiers in Earth Science*, 8, 2020.

S. Cherubini, G. De Cillis, O. Semeraro, S. Leonardi, and P. De Palma. Data driven modal decomposition of the wake behind an nrel-5mw wind turbine. *International Journal of Turbomachinery, Propulsion and Power*, 6(4), 2021.

A. T. Corey. Influence of shape on fall velocity of sand grains. *Unpublished MSc Thesis, Colorado AM College*, page 102 pp, 1949.

P. Corso, G. Giannakopoulos, U. Gulan, C. E. Frouzakis, and M. Holzner. A novel estimation approach of pressure gradient and haemodynamic stresses as indicators of pathological aortic flow using subvoxel modelling. *IEEE Transactions on Biomedical Engineering*, 68: 980–991, 2021.

C. Cummins, M. Seale, A. Macente, D. Certini, E. Mastropaolo, I. M. Viola, and N. Nakayama. A separated vortex ring underlies the flight of the dandelion. *Nature*, 562:414–418, 2018.

R. De Schryver. Dynamic mode decomposition in hydrodynamics: Influence of noise and missing data. *University of Gent, Department of Civil Engineering*, 2016.

P. A. Durbin and G. Medic. *Fluid Dynamics with a Computational Perspective*. Cambridge University Press, 2007.

A. Emadzadeh and Y. M. Chiew. Settling velocity of porous spherical particles. *Journal of Hydraulic Engineering*, 146(1):04019046, 2020.

L. B. Esteban, J. Shrimpton, and B. Ganapathisubramani. Three dimensional wakes of freely falling planar polygons. *Experiments in Fluids*, 60, 2019.

S. B. Field, M. G. Moore, and F. Nori. Chaotic dynamics of falling disks. *Nature*, 388: 252–254, 1997.

G. Gai and A. Wachs. On the dynamics and wakes of a freely settling platonic polyhedron in a quiescent newtonian fluid. *Journal of Fluid Mechanics*, 985:A3, 2024.

M. Geier and M. Arienti. Detection of preferential particle orientation in the atmosphere: Development of an alternative polarization lidar system. *Journal of Quantitative Spectroscopy and Radiative Transfer*, 149:16–32, 2014.

M. B. Giles and R. M. Cummings. Wake integration for three-dimensional flowfield computations: Theoretical development. *Journal of Aircraft*, 36(2):357–365, 1999.

K. L. S. Gunn and J. S. Marshall. The distribution with size of aggregate snowflakes. *Journal of Meteorology*, 15:452–461, 1957.

G. Huang, Y. Dai, and C.) Yang. Energy extraction in the dynamic modes of flow for airfoil's laminar separation flutter. *Physics of Fluids*, 34(8):083601, 08 2022.

K. Kikuchi, T. Kameda, K. Higuchi, and A. Yamasita. A Global Classification of Snow Crystals, Ice Crystals, and Solid Precipitation Based on Observations From Middle Latitudes to Polar Regions. *Atmospheric Research*, 132:460–472, 2013.

T. Kim, J. Chang, and D. Kim. Free-fall Dynamics of a Pair of Rigidly Linked Disks. *Physics of Fluids*, 30:034104, 2018.

T. Krake, D. Weiskopf, and B. Eberhardt. Dynamic mode decomposition: Theory and data reconstruction. 2019.

J. N. Kutz, X. Fu, and S. L. Brunton. Multi-Resolution Dynamic Mode Decomposition. *Journal on Applied Dynamical Systems*, 15:713–735, 2015.

k. Köbschal, J. Breitenbach, I.V. Roisman, C. Tropea, and J. Hussong. Geometric descriptors for the prediction of snowflake drag. 64:4, 2023.

S. B. Leask and V. G. McDonell. On the physical interpretation of proper orthogonal decomposition and dynamic mode decomposition for liquid injection. 2019.

C. Li, K. Lim, T. Berk, A. Abraham, M. Heisel, M. Guala, F. Coletti, and J. Hong. Settling and clustering of snow particles in atmospheric turbulence. *Journal of Fluid Mechanics*, 912:A49, 2021.

K. G. Libbrecht. The physics of snow crystals. *Reports on Progress in Physics*, 68(4):855–895, 2005.

J. L. Lumley. The Structure of Inhomogeneous Turbulent Flows. *Proceedings of the International Colloquium on the Fine Scale Structure of the Atmosphere and Its Influence on Radio Wave Propagation*, page 231, 1967.

M. W. McCorquodale and C. D. Westbrook. TRAIL: A Novel Experimental Approach for Studying the Aerodynamics of Ice Particles. *Quarterly Journal of the Royal Meteorological Society*, 2020a.

M. W. McCorquodale and C. D. Westbrook. TRAIL part 2: A Comprehensive Assessment of Ice Particle Fall Speed Parametrisations. *Quarterly Journal of the Royal Meteorological Society*, 2020b.

K. Menon and R. Mittal. Dynamic mode decomposition based analysis of flow over a sinusoidally pitching airfoil. *Journal of Fluids and Structures*, 94:102886, 2020. ISSN 0889-9746.

J. Nediç, O. Supponen, B. Ganapathisubramani, and J. C. Vassilicos. Geometrical influence on vortex shedding in turbulent axisymmetric wakes. *Physics of Fluids*, 27, 2015.

A. Nemes, T. Dasari, J. Hong, M. Guala, and F. Coletti. Snowflakes in the Atmospheric Surface Layer: Observation of Particle-Turbulence Dynamics. *Journal of Fluid Mechanics*, 814:592–613, 2017.

OpenFOAM. *User Guide - OpenFOAM 5.0*. 2017.

P. J. Schmid. Dynamic mode decomposition of numerical and experimental data. *Journal of Fluid Mechanics*, 656:5–28, 2010.

D. K. Singh, E. R. Pardyjak, and T. J. Garrett. A universal scaling law for Lagrangian snowflake accelerations in atmospheric turbulence. *Physics of Fluids*, 35(12):123336, 2023.

P. Spalart and S. Allmaras. A one-equation turbulence model for aerodynamic flows. *AIAA Paper*, 1:5–21, 1994.

P. R. Spalart, S. Deck, M. L. Shur, K. D. Squires, M. K. Strelets, and A. Travin. A New Version of Detached-Eddy Simulation, Resistant to Ambiguous Grid Densities. *Theoretical and Computational Fluid Dynamics*, 20:180, 2006.

J. Sánchez-Rodríguez and F. Gallaire. Tumbling elimination induced by permeability: an experimental approach. 2024.

G. Tagliavini. *Computational investigation of complex-shaped snow particle aerodynamics: drag prediction and wake characteristics*. ETH Zurich, 2022.

G. Tagliavini, M. McCorquodale, C. Westbrook, P. Corso, Q. Krol, and M. Holzner. Drag coefficient prediction of complex-shaped snow particles falling in air beyond the Stokes regime. *International Journal of Multiphase Flow*, 140:103652, 2021a.

G. Tagliavini, M. McCorquodale, C. Westbrook, and M. Holzner. Numerical analysis of the wake of complex-shaped snow particles at moderate Reynolds number. *Physics of Fluids*, 33(10):105103, 2021b.

K. Taira, S. L. Brunton, S. T. M. Dawson, C. W. Rowley, T. Colonius, B. J. McKeon, O. T. Schmidt, S. Gordeyev, V. Theofilis, and L. S. Ukeiley. Modal analysis of fluid flows: An overview. *AIAA Journal*, 55(12):4013–4041, 2017.

G. Tissot, L. Cordier, N. Benard, and B. R. Noack. Model reduction using dynamic mode decomposition. *Comptes Rendus Mécanique*, 342(6):410–416, 2014.

C. Toupoint, P. Ern, and V. Roig. Kinematics and Wake of Freely Falling Cylinders at Moderate Reynolds Numbers. *Journal of Fluid Mechanics*, 866:21–32, 2019.

R. Trunk, C. Bretl, G. Thäter, H. Nirschl, M. Dorn, and M. J. Krause. A Study on Shape-Dependent Settling of Single Particles with Equal Volume Using Surface Resolved Simulations. *Computation*, 9:40, 2021.

J. H. Tu, C. W. Rowley, D. M. Luchtenburg, S. L. Burton, and N. Kutz. On dynamic mode decomposition: Theory and applications. *Journal of Computational Dynamics*, 1(2): 391–421, 2014.

M. Uhlmann and J. Dusek. The Motion of a Single Heavy Sphere in Ambient Fluid: a Benchmark for Interface-Resolved Particulate Flow Simulations with Significant Relative Velocities. *International Journal of Multiphase Flow*, 50:221–243, 2014.

J. M. Vega and S. Le Clainche. Higher Order Dynamic Mode Decomposition. *Journal on Applied Dynamical Systems*, 16:882–925, 2017.

P. Welch. The use of fast fourier transform for the estimation of power spectra: A method based on time averaging over short, modified periodograms. *IEEE Transactions on Audio and Electroacoustics*, 15(2):70–73, 1967.

C. D. Westbrook. The Fall Speeds of Sub-100 microns Ice Crystals. *Quarterly Journal of the Royal Meteorological Society*, 134:1243–1251, 2008.

P. Yu and V. Durgesh. Modal decomposition techniques: Application in coherent structures for a saccular aneurysm model. *Fluids*, 7(5), 2022.

Supplementary Files

This is a list of supplementary files associated with this preprint. Click to download.

- suppMatGTagliavini.pdf